JGR Space Physics

RESEARCH ARTICLE
10.1029/2019JA027433

Updated Neutron-Monitor Yield Function: Bridging Between In Situ and Ground-Based Cosmic Ray Measurements

Alexander L. Mishev[1,2], Sergey A. Koldobskiy[1,3], Gennady A. Kovaltsov[4], Agnieszka Gil[5,6], and Ilya G. Usoskin[1,2]

[1]Space Physics and Astronomy Research Unit, University of Oulu, Oulu, Finland, [2]Sodankylä Geophysical Observatory, University of Oulu, Oulu, Finland, [3]National Research Nuclear University "MEPhI", Moscow, Russia, [4]Ioffe Physical-Technical Institute, St. Petersburg, Russia, [5]Space Research Center, Polish Academy of Sciences, Warsaw, Poland, [6]Institute of Mathematics, Siedlce University, Siedlce, Poland

Key Points:
- Yield function of a standard NM64 neutron monitor is updated to cover the full range of altitudes, from sea level to 500 g/cm^2
- The yield function is validated using direct cosmic ray spectrum measurements by AMS-02 experiment
- Stability of the available NM64 neutron monitors is assessed for the period May 2011 through May 2017

Supporting Information:
- Supporting Information S1

Correspondence to:
I. G. Usoskin,
ilya.usoskin@oulu.fi

Citation:
Mishev, A. L., Koldobskiy, S. A., Kovaltsov, G. A., Gil, A., & Usoskin, I. G. (2020). Updated neutron-monitor yield function: Bridging between in situ and ground-based cosmic ray measurements. *Journal of Geophysical Research: Space Physics*, *125*, e2019JA027433. https://doi.org/10.1029/2019JA027433

Received 19 SEP 2019
Accepted 23 JAN 2020
Accepted article online 10 FEB 2020

Abstract An updated yield function for a standard NM64 neutron monitor (NM) is computed and extended to different atmospheric depths from sea level to 500 g/cm^2 (~5.7 km altitude) and is presented as lookup tables and a full parametrization. The yield function was validated using the cosmic ray spectra directly measured in space by the AMS-02 experiment during the period May 2011 through May 2017 and confronted with count rates of all NM64-type NMs being in operation during this period. Using this approach, stability of all the selected NMs was analyzed for the period 2011–2017. Most of NMs appear very stable and suitable for studies of long-term solar modulation of cosmic rays. However, some NMs suffer from instabilities like trends, apparent jumps, or strong seasonal waves in the count rates.

1. Introduction

Ground-based detectors of cosmic rays (CRs), namely, neutron monitors (NMs), are the primary instrument to monitor CR variability on long-term scale (since the 1950s) and also to study strong interplanetary transients and the most energetic solar particle events (Simpson, 2000). Although a single NM is an energy-integrating detector, unable to resolve the spectrum of CRs, the worldwide network of NMs, located at different latitudes and altitudes, forms a basic spectrometer in the energy range below ≈15 GeV (e.g., Moraal et al., 2000). However, because of the thickness of the Earth's atmosphere, primary particles cannot reach the detector but initiate a nucleonic-muon-electromagnetic cascade in the atmosphere so that only secondary products of the cascade, mostly hadrons, are measured by the ground-based detectors (Clem & Dorman, 2000). In order to study CR variability using ground-based detectors, this complicated process needs to be precisely known and modeled. Modeling of the CR-induced atmospheric cascade is typically done by Monte Carlo simulations as pioneered by Debrunner and Brunberg (1968) and quantified in terms of the yield function (YF) of a NM, details are given in section 2. NM YF incorporates the full complexity of the atmospheric cascade development and secondary-particle propagation through the Earth's atmosphere as well as the efficiency of the detector itself to register the secondaries.

Although (semi)empirical parameterization of latitude survey observations was used earlier to determine the YF (e.g., Caballero-Lopez & Moraal, 2012; Lockwood et al., 1974; Nagashima et al., 1989), modern state-of-the-art models for the YF (Clem & Dorman, 2000; Mangeard et al., 2016; Mishev et al., 2013) are based on Monte Carlo tools but still exhibit a degree of discrepancy between each other, especially in the low-energy range (Koldobskiy et al., 2019). Comparison between direct CR spectral measurements and NM responses (Gil et al., 2015; Koldobskiy et al., 2018, 2019) has shown that YF by Mishev et al. (2013) is most consistent with the observational data. However, this YF, as well as some other YFs, was determined for sea level, while many NMs are located at middle and high altitudes. Therefore, the use of these YFs was limited to low-altitude NMs only. Considering the altitude effect as a simple barometric correction is not appropriate, especially if the correction is comparable to or exceeds one attenuation length (Flückiger et al., 2008).

Here we update the YF by Mishev et al. (2013) and expand it to higher altitudes, from sea level up to 500 g/cm^2 of the residual atmospheric depth (or ~5.7 km altitude) and validate it using data from different

©2020. American Geophysical Union. All Rights Reserved.

Table 1
Computed Yield Function, in Units of (m^2 sr), of a Standard 6NM64 Neutron Monitor Located at the Given Atmospheric Depth h for the Unity Isotropic Flux of Primary Protons With the Fixed Energy as Indicated in Column 1

	Atmospheric depth h (g/cm^2)					
E_p (GeV)	1,000[a]	900	800	700	600	500
0.12	7.17E−12	3.66E−11	1.56E−10	5.88E−10	2.09E−9	7.52E−9
0.23	7.32E−9	3.06E−8	1.13E−7	3.85E−7	1.26E−6	4.17E−6
0.43	8.46E−6	2.96E−5	9.60E−5	2.96E−4	8.93E−4	2.70E−3
1.27	1.21E−3	3.27E−3	8.69E−3	2.27E−2	5.89E−2	1.51E−1
2.21	5.42E−3	1.33E−2	3.23E−2	7.79E−2	1.86E−1	4.38E−1
4.15	2.00E−2	4.51E−2	1.01E−1	2.23E−1	4.85E−1	1.03E+0
9.11	1.09E−1	2.31E−1	4.77E−1	9.60E−1	1.88E+0	3.60E+0
19.1	2.29E−1	4.69E−1	9.18E−1	1.73E+0	3.15E+0	5.60E+0
29.1	—	6.53E−1	1.25E+0	2.28E+0	4.05E+0	7.03E+0
49.1	5.90E−1	1.14E+0	2.10E+0	3.75E+0	6.64E+0	1.15E+1
69.1	—	1.37E+0	2.47E+0	4.38E+0	7.68E+0	1.34E+1
99.1	9.92E-1	1.73E+0	3.02E+0	5.33E+0	9.32E+0	1.61E+1
299.1	—	3.95E+0	6.56E+0	1.15E+1	1.98E+1	3.41E+1
499.1	3.35E+0	5.25E+0	8.39E+0	1.45E+1	2.48E+1	4.23E+1
699.1	—	6.44E+0	9.94E+0	1.71E+1	2.88E+1	4.89E+1
999.1	6.67E+0	9.97E+0	1.53E+1	2.58E+1	4.28E+1	7.20E+1

[a]Values from Mishev et al. (2013).

NMs and the CR spectra directly recorded in space by the Alpha Magnetic Spectrometer AMS-02 experiment (Aguilar et al., 2018). We also verify the stability of all NMs operating during the period of 2011–2017 covered by the AMS-02 data.

2. NM Yield Function

The theoretical response of a NM to CRs is determined as integral of the product of the CR spectrum and the NM YF so that the count rate of a NM at any time t can be computed as

$$N(P_c, h, t) = \sum_i \int_{E_{c,i}}^{\infty} Y_i(E, h) \quad J_i(E, t) \quad dE, \tag{1}$$

where P_c is the local geomagnetic cutoff rigidity (Cooke et al., 1991; Smart et al., 2006), h is the atmospheric depth (or altitude), integration is over the CR kinetic energy per nucleon, and the summation is over different types i of the primary CR particles (protons, helium, etc.). The term $Y_i(E, h)$ [m^2 sr/nuc] represents the YF of a NM for primaries of particle type i, while $J_i(E, t)$ nucleons per [GeV/nuc m^2 sr s] is the energy spectrum of nucleons of primary particle of type i (with charge and mass numbers Z_i and A_i, respectively) at time t, $E_{c,i} = \sqrt{Z_i^2 \cdot P_c^2/A_i^2 + E_0^2} - E_0$, where $E_0 = 0.938$ GeV is the proton's rest mass. The NM YF can be generally defined as (e.g., Flückiger et al., 2008)

$$Y_i(E, h) = G(E) \sum_j \int \int S_j(E', \theta) \cdot F_{i,j}(E, h, E', \theta) \quad dE' \quad d\Omega, \tag{2}$$

where $G(E)$ is the geometrical correction factor; $S_j(E', \theta)$ is the detector's response function, equal to the geometrical area times the registration efficiency for a secondary particle of type j with energy E' impinging on the detector with the zenith angle θ; $F_{i,j}(E, h, E', \theta)$ is the differential flux of secondary particles of type j (neutrons, protons, muons, and pions) for a primary particle of type i with kinetic energy per nucleon E, impinging isotropically on the top of the atmosphere; and the integration is over the energy of secondary particles E' and solid angle Ω. The geometrical correction, accounting for the finite lateral expansion of the CR-induced atmospheric cascades and the detector's electronic dead time, was first introduced by Mishev

Table 2
Computed Yield Function, in Units of (m^2 sr nuc^{-1}), of a Standard 6NM64 Neutron Monitor Located at the Given Atmospheric Depth h for the Unity Isotropic Flux of Primary α Particles With the Fixed Energy Per Nucleon as Indicated in Column 1

E_a	Atmospheric depth h (g/cm^2)					
(GeV/nuc)	1,000	900	800	700	600	500
0.5	1.32E−4	5.46E−4	1.45E−3	4.38E−3	1.29E−2	3.84E−2
1	1.54E−3	4.37E−3	1.07E−2	2.88E−2	7.71E−2	2.05E−1
2	8.64E−3	2.15E−2	4.97E−2	1.22E−1	2.95E−1	7.06E−1
3	1.72E−2	4.03E−2	9.01E−2	2.08E−1	4.74E−1	1.06E+0
5	4.72E−2	1.04E−1	2.04E−1	4.41E−1	9.34E−1	1.94E+0
10	8.37E−2	1.76E−1	3.64E−1	7.55E−1	1.47E+0	2.77E+0
20	2.15E−1	4.40E−1	8.60E−1	1.73E+0	3.15E+0	5.60E+0
29.1	—	6.53E−1	1.25E+0	2.28E+0	4.05E+0	7.03E+0
49.1	5.90E−1	1.14E+0	2.10E+0	3.75E+0	6.64E+0	1.15E+1
69.1	—	1.37E+0	2.47E+0	4.38E+0	7.68E+0	1.34E+1
99.1	9.92E−1	1.73E+0	3.02E+0	5.33E+0	9.32E+0	1.61E+1
299.1	—	3.95E+0	6.56E+0	1.15E+1	1.98E+1	3.41E+1
499.1	3.35E+0	5.25E+0	8.39E+0	1.45E+1	2.48E+1	4.23E+1
699.1	—	6.44E+0	9.94E+0	1.71E+1	2.88E+1	4.89E+1
999.1	6.67E+0	9.97E+0	1.53E+1	2.58E+1	4.28E+1	7.20E+1

Note. The YF for α particles is provided per nucleon.
[a]Values from Mishev et al. (2013).

et al. (2013) and is applied here in the same way. It is essential at energies >10 GeV/nuc of the primary particles and depends on the altitude due to specifics of cascade development affecting the lateral distribution of secondary particles (Engel et al., 2011). All the computations were done for the standard 6NM64 NM (Hatton & Carimichael, 1964; Moraal et al., 2000; Stoker et al., 2000). Another, original type of NM, called IGY (Simpson, 2000), was the primary type of detectors before 1964 and is not considered here, since it has different sensitivity to secondary particles (Simpson, 2000; Stoker et al., 2000). Accordingly, a new full computation of the IGY-type detector response is needed to achieve the precision aimed here, and this is planned for a subsequent work.

2.1. Monte Carlo Simulation

Propagation and interaction of primary particles in the atmosphere were simulated with the PLANETOCOSMICS simulation tool (Desorgher et al., 2005) based on the GEANT4 package (Agostinelli et al., 2003), applying the NRLMSISE-00 atmospheric model (Picone et al., 2002). The simulation scheme was the same as in Mishev et al. (2013).

First we calculated, by means of the PLANETOCOSMICS code, fluxes of all types of secondary particles at prescribed atmospheric depths and then convoluted them with the registration efficiency (equation (2)). Here we used the NM registration efficiency according to Clem and Dorman (2000) and Maurchev and Balabin (2016), considering secondary neutrons, protons, positive and negative pions, and muons that contribute to the counts of the device (Clem & Dorman, 2000; Mishev et al., 2013). The computations were carried out separately for primary protons and α particles with isotropic incidence in a wide energy range from about 0.5 GeV/nuc to 1 TeV/nuc. Heavier ($Z > 2$) CR species can be effectively represented by α particles, scaled according to the number of nucleons, with the same energy per nucleon (e.g., Engel et al., 2011; Usoskin & Kovaltsov, 2006).

The results of the computations are given as lookup tables (see Tables 1 and 2) for different atmospheric depths between sea level and 500 g/cm^2 for primary protons and α particles, respectively. The YF for α particles is provided per nucleon. Parameterizations of the computed YFs are presented in section 2.2.

Figure 1 presents some results of the YF computed for several altitudes (atmospheric depths) from 1,000 g/cm^2, close to the mean sea level (1,033 g/cm^2) to 500 g/cm^2 (a high-mountain NM). These levels

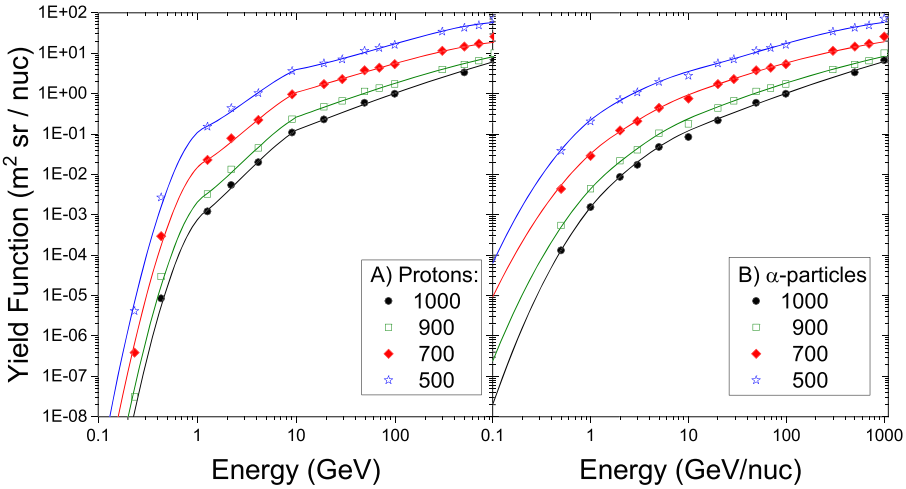

Figure 1. Yield function of a standard 6NM64 neutron monitor, located at different atmospheric depths h as indicated in the legend in units of g/cm^2, for primary protons (panel a) and α particles (panel b). Symbols represent the results of the Monte Carlo simulation for fixed energies (as tabulated in Tables 1 and 2, respectively), while curves correspond to the parameterization described in section 2.2.

encompass all possible NMs locations (Mavromichalaki et al., 2011). The result for sea level is nearly identical to that of Mishev et al. (2013). The computed YF is consistent with the results of NM latitude surveys, specifically in the low-energy range (Nuntiyakul et al., 2018).

2.2. Parametrization

Since the computational grid was not very dense (Tables 1 and 2), and a simple interpolation within the grid can lead to essential errors, we have developed a parametrization of the computed YF for a NM with the given atmospheric depth h (in g/cm^2) in the following form:

$$\ln\left(\frac{Y(h,E)}{Y(1{,}000,E)}\right) = A(R)\cdot(1{,}000-h)^2 + B(R)\cdot(1{,}000-h), \tag{3}$$

where E is energy per nucleon of the primary particle, and $Y(1{,}000, E)$ is the YF at the level of 1,000 g/cm^2, which is parameterized as a third-order polynomial of the parameter R defined as $R = \sqrt{E\cdot(E+1.876)}$, where E is kinetic energy in GeV per nucleon.

$$\ln(Y(1{,}000,E)) = \sum_{l=0}^{3} a_l(\ln(R))^l, \tag{4}$$

where Y is in [m^{2}sr/nuc], and coefficients are given in Table 3 in several energy ranges providing the best agreement with the directly calculated points.

Table 3
Coefficients of Equation (4) for Protons (Upper Block) and α Particles (Bottom Block)

a_3	a_2	a_1	a_0	E range
protons				
0	−8.6616	13.879	−12.104	$E \le 1.28$ GeV
−0.186	0.428	2.831	−8.76	$1.28 < E < 10$ GeV
0	−0.0365	1.206	−4.763	$E \ge 10$ GeV
α particles				
0.5082	−3.0659	7.2827	−9.5396	$E \le 1.7$ GeV/nuc
0.1179	−1.2022	4.9329	−8.65	$1.7 < E < 15$ GeV/nuc
0	−0.0365	1.206	−4.763	$E \ge 15$ GeV/nuc

Table 4
Coefficients of Equation (5) for Protons (Upper Block) and α particles (Bottom Block)

Coefficient	b_5	b_4	b_3	b_2	b_1	b_0
protons						
A	6.945E−09	−1.461E−07	1.115E−06	−3.402E−06	3.355E−06	−9.823E−07
B	−3.963E−06	8.091E−05	−6.394E−04	2.348E−03	−4.713E−03	1.186E−02
α particles						
A	9.422E−09	−2.284E−07	2.037E−06	−7.828E−06	1.203E−05	−5.545E−06
B	−5.351E−06	1.316E−04	−1.226E−03	5.176E−03	−1.017E−02	1.458E−02

Coefficients A and B in equation (3) are parameterized as a fifth-order polynomial:

$$A(R) \text{ (or } B(R)) = \sum_{l=0}^{5} b_l (\ln(R))^l, \tag{5}$$

where R is the same as in equation (4), and coefficients are given in Table 4.

Examples of the parametrization are shown in Figure 1. Overall, the accuracy of the parametrization (the difference between the computed and parametrized YF values) is within several percent, which is comparable to a typical uncertainty of the cascade simulation (Pierog, 2017).

3. Validation of the YF

Here we apply the new YF and the directly measured galactic cosmic ray (GCR) spectra to compute the expected NM count rates and compare those with NM observation. This can serve as a validation of the revisited YF and also as a test for the stability of different NMs over more than a half of the last solar cycle.

3.1. Data Selection

As the input spectra ($J_i(E,t)$ in equation (1)) we used spectra of protons and helium measured by AMS-02 experiment (Aguilar et al., 2018) for the period May 2011 through May 2017. The spectra were measured for 79 Bartels rotations (BR) 27 days each, 2,426–2,506. Heavier ($Z > 2$) species of GCR were included using the rigidity-dependent scaling of helium, as proposed by Koldobskiy et al. (2019). Thus, using these input parameters and the NM YF computed here, we calculated the theoretically expected count rates of all NM64-type NMs in operation during the time period considered, that is, for 79 BRs. For each NM, the atmospheric depth corresponding to the reference barometric pressure was used. We have also applied a simple median ±20% filter to the BR-averaged data to remove apparent outliers and jumps and then to calculate the BR-averaged count rates. Smaller-scale jumps cannot be removed in this way as comparable to the natural variability. Further on, we processed data, as they are provided not analyzing sources of the outliers or discontinuities.

The list of NMs used here is presented in Table 5 along with their main parameters such as altitude, geomagnetic cutoff rigidity, and scaling factor (see below). We checked all NMs operational during at least half (≥40 BR) of the analyzed time interval. The NM data for the analyzed time intervals were collected using different sources: Neutron Monitor Data Base (http://nmdb.eu), IZMIRAN database (http://cr0.izmiran.ru/common/links.htm), and dedicated web servers for Oulu NM and Apatity NM. We point out that the data from different sources may differ for some NMs. This is mostly due to inconsistencies in the normalization coefficients or the number of counters indicated in the NM's metadata, but sometimes, there are also apparent jumps or gaps in one of the sources but not in the other. We analyzed all sources for each NM and selected those with the visually most stable data. The data sources used for each NM data set are indicated in Table 5.

3.2. Validation Procedure

Using the spectra of GCR measured by AMS-02 for individual BR periods and the YF presented above, we have calculated the theoretically expected count rate N_{th} for the selected NMs, using equation (1). Then the expected count rates were confronted with the actually measured count rates (corrected for the pressure and efficiency) of these NMs, N_{m} for the same periods. Because of the nonideality of a NM, namely,

Table 5
List of Neutron Monitors Analyzed Here

Name	Source	P_c (GV)	p_0 (mb)	n	κ	Stability
AATB	1	5.95	675	79	1.338	J, T(0.7)
APTY[a]	3	0.45	1,010	79	1.193	Stable
ATHN	1	8.53	980	79	1.152	Stable
BJNG	2	8.8	1,000	46	1.098	T(−0.3)
BKSN	2	5.6	820	76	1.149	J
BRBG	2	0.0	1,000	79	1.365	T(−0.5)
CALM	1	6.95	1,000	64	2.124	Stable
DJON	1	11.22	1,001.3	68	1.019	Stable
DRBS	1	3.34	986.6	72	1.098	J
ESOI	2	10.2	800	75	1.053	S(>5%)
FSMT	1	0.3	1,013	79	0.947	Stable, S(2%)
HRMS	1	4.44	1,013.25	79	1.045	Stable
INVK	1	0.3	1,013	79	1.059	Stable
IRK2	2	3.13	800	75	1.508	J
IRK3	2	3.51	715	60	1.294	J
JUN1	1	4.49	642.614	79	1.184	J, S(10%)
KERG	1	1.14	1,000	77	0.998	Stable
KIEL[b]	1	2.21	1,006.7	79	1.184	J, T(−0.3)
LMKS	2	3.84	733.3	75	1.454	J, T(−0.5)
MCMD	1	0.3	973.25	75	1.304	Stable
MGDN	1	1.78	982.2	54	1.423	J, T(0.3)
MOSC	1	2.13	1,000	79	1.197	Stable
MRNY	2	0.03	1,013	79	1.118	T(0.3)
MWSN	2	0.22	990	78	0.921	Stable
MXCO	2	8.28	778.58	79	1.135	Stable
NAIN	1	0.3	1,013	79	0.952	Stable
NANM	1	7.1	802	76	1.512	J, T(1.0)
NRLK	2	0.45	1,005	66	1.227	J, T(0.3)
NVBK	2	2.4	995	79	0.977	T(−0.4)
NWRK	1	2.4	1,013.3	79	1.039	Stable
OULU	4	0.62	1,000	79	1.047	Stable
PSNM	2	16.8	750.479	79	0.883	Stable
PWNK	1	0.3	1,013.3	79	0.943	Stable
ROME	1	6.27	1,009.25	63	1.290	Stable
SNAE	1	0.73	880	79	1.072	Stable
SOPO	1	0.1	680	79	1.247	Stable
TERA	1	0.0	986.42	79	1.063	Stable
THUL	1	0.3	1,005	79	1.759	Stable
TIBT	1	13.44	607	66	0.828	Stable
TSMB	1	8.95	880	73	1.120	Stable
TXBY	2	0.48	1,000	79	1.360	S(3%), J
YKTK	2	1.37	1,000	75	1.303	T(−0.6)

Note. Columns are NM standard abbreviation (full name and location information can be found at http://cidas.isee.nagoya-u.ac.jp/WDCCR/station&urluscore;list.php); source of data: (1) NMDB, http://www.nmdb.eu; (2) IZMIRAN, http://cr0.izmiran.ru/common/links.htm; (3) http://pgia.ru/data/nm; (4) http://cosmicrays.oulu.fi); effective vertical geomagnetic cutoff rigidity P_c for the 2015 epoch; reference barometric pressure p_0; the number of Bartels rotations analyzed, n; the obtained mean scaling factors κ (see text); and an assessment of the NM stability during the period May 2011 to May 2017 (notations: J = apparent jumps; S = seasonal wave; T = trend in units of %/year). [a]Short dead time. [b]Applied as KIEL2 corrected by 5% (see http://www.nmdb.eu/station/kiel/).

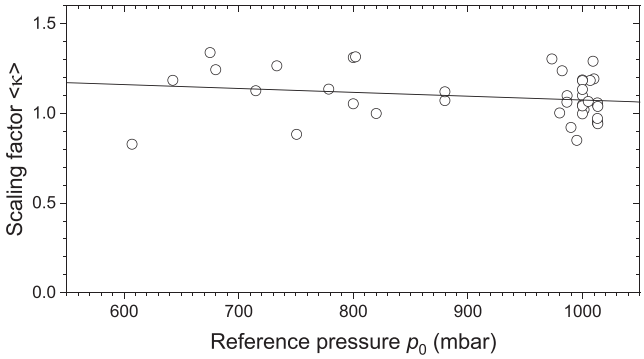

Figure 2. The mean scaling factor $\langle\kappa\rangle$ of individual NM64 detectors (SNM15-type detectors were scaled down by 15%, see Abunin et al., 2011) as function of the reference atmospheric pressure of the NM location. The two outliers, CALM and THUL, are excluded. The line depicts the best fit linear regression, which is consistent with no dependence.

electronic setups, very local environment (materials, electronics, and existing construction), efficiency of counter tubes, and so forth, the expected count rates are not always equal to the real ones but are typically proportional to that (see, e.g., Koldobskiy et al., 2019; Usoskin et al., 2017), via the so-called scaling factor, which is defined as

$$\kappa = \frac{N_{\mathrm{th}}}{N_{\mathrm{m}}}. \tag{6}$$

The higher is the scaling κ factor, the lower is the measured count rate of a given NM in comparison with the "ideal" NM. Normally, one would expect that the value of κ is close to unity. We note that the YF was computed for the reference 6NM64 NM using the standard counters BP28 produced at the Chalk River laboratory (Hatton & Carimichael, 1964). For the APTY NM we used the data with the short dead time (0.01 ms) corresponding to the standard NM64 setup, while the long dead-time (1.2 ms) data set was ignored (see details in http://pgia.ru/data/nm). On the other hand, some detectors, mostly from the former Soviet Union and East Europe, are based on Soviet analogs of these counters, called SNM-15, which have slightly lower (by 15–20%) efficiency, and thus higher κ, because of the lower purity of the filling gas $^{10}BF_3$ (Gil et al., 2015; Abunin et al., 2011). The values of κ were calculated for each NM for each BR and further analyzed for their stability in time.

The mean scaling factor over the entire period $\langle\kappa\rangle$ was found (see Column 6 in Table 5) to be consistent with our expectations, namely, close to unity within ±25% (additionally accounting for the 15% lower efficiency of SNM15-type counters). Only two NMs deviate from this, showing a high value of $\langle\kappa\rangle$: CALM (2.12) and THUL (1.76). This may imply either a halved efficiency of the detectors or an error in the metadata (e.g., incorrect number or type of counters) for these NMs in the databases. Figure 2 shows dependence of the mean $\langle\kappa\rangle$ values (SNM15-type ones were reduced by 15% to allow compensation for the lower registration efficiency) on the reference pressure of the analyzed NM (except for CALM and THUL as mentioned above). The scaling factor is consistent with no dependence on the NM location height—the regression line shown in Figure 2 has the slope of $(-2 \pm 2) \cdot 10^{-4}$ mb^{-1}. This implies that the altitude dependence of the NM YF is treated correctly in our simulations.

Further on, we also analyzed the stability of different NMs throughout the entire period of 2011–2017. Some examples of the analysis are shown in Figure 3, while the full set of plots can be found in the supporting information. The left-hand side (LHS) panels depict scatter plots of N_{m} versus N_{th} (each dot corresponds to one BR) along with the mean proportionality (red line) and its 68% confidence interval (red shaded area). The right-hand side (RHS) panels depict the "momentary" (i.e., calculated for each BR individually) scaling factor κ. The mean $\langle\kappa\rangle$ and its standard error are shown in the upper-right corner. This analysis allows one to assess the stability of each NM over the studied time period of 2011–2017.

The top panel of Figure 3 corresponds to the very stable OULU (Oulu, Finland) NM, where one can see that the points in the LHS panel lie tightly along the linear scaling $\langle\kappa\rangle = 1.047$ and the individual κ values (RHS panel) depict a stable behavior, varying within 0.01 around the mean without any apparent trend (the

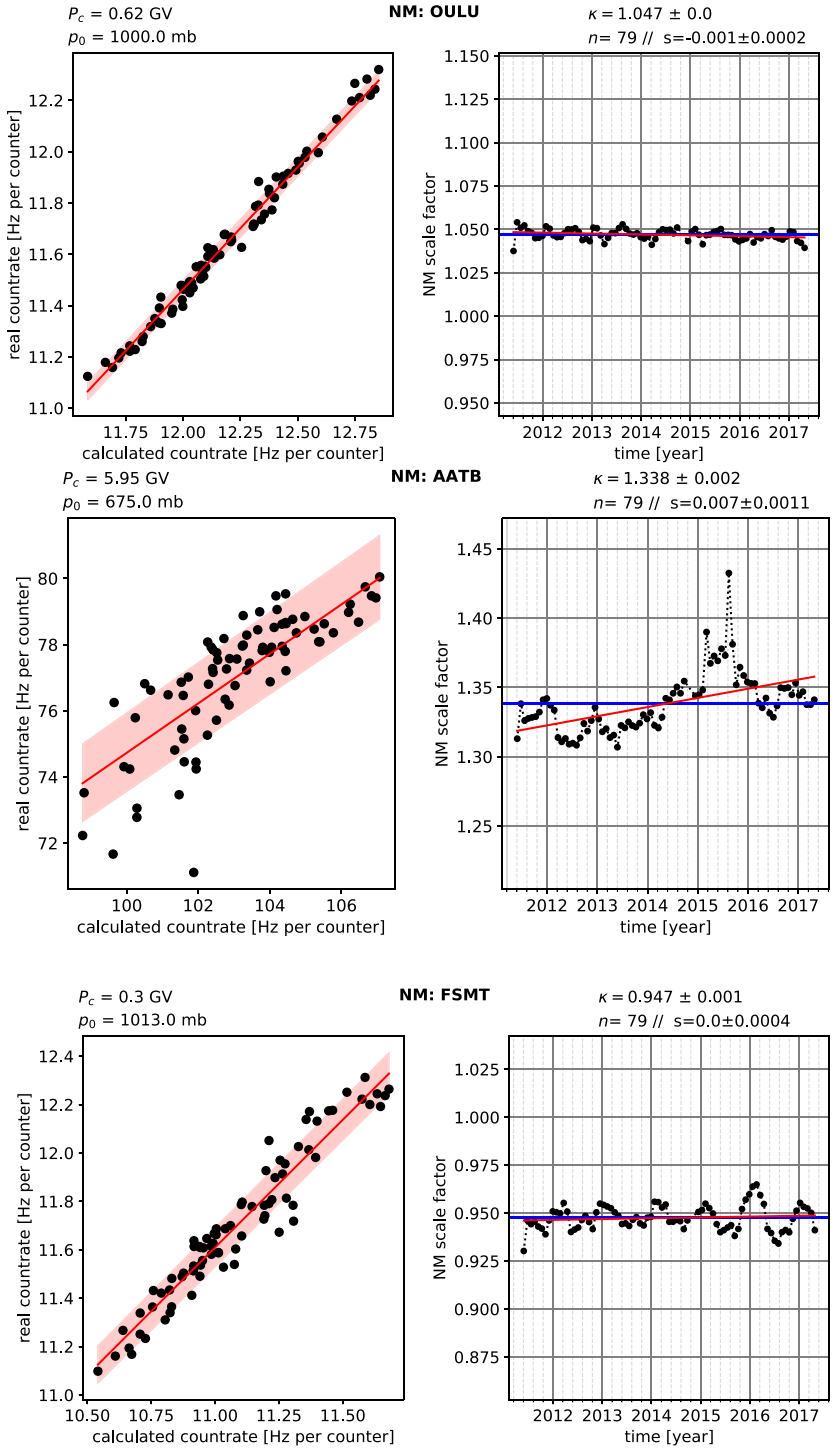

Figure 3. Examples of the analysis of OULU, AATB, and FSMT NMs (top, middle, and bottom panels, respectively). Headers indicate the NM name, cutoff rigidity P_c, reference pressure p_0, the mean scaling factor κ with the standard error of the mean, number of Bartels rotation intervals n used in the analysis, and the slope s (in year^{-1}) of κ versus time. Left-hand panels depict scatter plots of recorded versus calculated NM count rates, where each point corresponds to one Bartels rotation; the red line with the shaded strip depicts the linear scaling regression κ with the 68% confidence interval. Right-hand panels depict the values of κ for individual Bartels rotations (black dots), the mean κ value (blue line), and the linear slope of κ versus time (red line). OULU NM exhibits a stable behavior. AATB – trend and jumps; FSMT – seasonal wave.

formal trend is insignificant and less than 0.1% per year), jumps, or systematic patterns. Thus, the OULU NM is considered as stable, and this is indicated in the last column of Table 5.

The middle panel of Figure 3 corresponds to the AATB (Alma-Ata B, Kazakhstan) NM, whose performance is unstable during the analyzed period. As one can see on the RHS plot, the κ values exhibit systematic trend, indicated by the red line, and apparent jumps, leading to a wide spread of points in the LHS panel. Thus, the highly significant trend ($\approx 0.7 \pm 0.1\%$ per year) and the jumps are indicated for this NM in Table 5.

The bottom panel of Figure 3 corresponds to the FSMT (Fort Smith, Canada) NM, whose performance is stable but exhibits a moderate seasonal wave of about 3% magnitude, as likely related to the snow effect during winters. This is also indicated in Table 5.

All other NMs were assessed in a similar way (see the plots in the supporting information), with the assessment results being summarized in the last column of Table 5. Most NMs were found stable during the period of 2011–2017, but some specific cases are discussed below:

- BJNG NM (Beijing, China) exhibits a trend of $\approx$0.3%/year;
- BKSN NM (Baksan, Russia) exhibits significant apparent jumps;
- BRBG NM (Barentsburg, Norway, operated by Russia) has a clear trend of about −0.4%/year;
- DRBS NM (Dourbes, Belgium) exhibits significant apparent jumps;
- ESOI NM (Mt. Hermon, Israel) suffers from severe seasonal cycles caused by snow in the winter seasons;
- IRK2/IRK3 NMs (Irkutsk, Russia) exhibit significant apparent jumps;
- JUN1 NM (Jungfraujoch, Switzerland) exhibits a strong (~10%) seasonal cycle and jumps, related to the snow cover;
- KIEL NM (Kiel, Germany) data contains a few apparent jumps and a moderate trend (≈ -0.3%/year);
- LMSK NM (Lomnicky Štit, Slovakia) exhibits an apparent trend and a few jumps;
- MGDN NM (Magadan, Russia) exhibits some moderate jumps and a trend in data;
- MRNY NM (Mirny, Antractica, operated by Russia) has a trend, probably caused by a jump in late 2013, and a small seasonal wave;
- NANM NM (Nor-Amberd, Armenia) exhibits a strong trend and several big jumps;
- NRLK NM (Norilsk, Russia) data are distorted by apparent big jumps;
- NVBK NM (Novisibirsk, Russia) exhibits a clear trend of ≈ -0.4%/year;
- SOPO NM (South Pole, operated by USA) depicts a weak trend of ≈ -0.2%/year, which is insignificant on the 6-year interval analyzed here, and disagrees with the long-term drift found for the SOPO NM (Bieber et al., 2013);
- TXBY NM (Tixie Bay, Russia) data exhibit a strong seasonal wave and a big jump toward the end of the time interval;
- YKTK NM (Yakutsk, Russia) exhibits an apparent trend of ≈ -0.5%/year.

As stable we considered NMs without apparent jumps and with trends being consistent with the no-trend hypothesis. We note that here we do not distinguish between real instability of the detectors and possible glitches in the database but we only assess the quality of the available official data from the user's point of view.

4. Summary and Conclusions

An updated YF with the corresponding parametrization is presented for the standard 6NM64 for both primary protons and α particles. The approach is based on the previously published YF (Mishev et al., 2013) for sea level and isotropic flux of CR particles but extended here to different altitudes/atmospheric depths from sea level to 500 g/cm^2. The updated YF was computed by Monte Carlo simulations with a high statistical performance. Both lookup tables and the parametrization of the updated YF are presented here.

We have validated the updated YF by applying it to the CR spectra directly measured in space by the AMS-02 experiment for 79 BR (27-day) intervals during the period May 2011 through May 2017 and confronted the results with count rates of all NM64 NMs being in operation during this period. In this way, the updated YF was validated, including its altitude dependence. The scaling factor κ, which quantifies the "nonideality" of a detector, was calculated for each NM (see Table 5). It appears to be close to unity within 25% with no statistical dependence on the atmospheric depth, thus confirming the overall correctness of the NM YF for different altitudes presented in this paper.

Using the new YF and the directly measured CR spectra, we also assessed stability of all the selected NMs as summarized in Table 5. Most of NMs demonstrate very stable operation during the period 2011–2017 and are thus suitable for studies of long-term solar modulation of CRs, at least during this period. But of course, the present analysis cannot evaluate the NM stability beyond this time interval. However, some NMs were found to suffer from such instabilities as trends in data, apparent jumps in the count rate, or a strong seasonal wave. Data from these NMs are not recommended to be directly used for a long-term analysis, or cautions should be taken to deal with the instabilities.

In conclusion, a newly updated YF of a standard NM64 NM, covering the entire range of locations, from sea level to the atmospheric depth of 500 g/cm^2, was computed and validated via CR spectra directly measured in space by the AMS-02 experiment for the period May 2011 through May 2017. The new YF is tabulated and parameterized and is ready to use. Using the updated YF, stability of all NMs was assessed for this time interval.

Acknowledgments
Data of AMS-02 were obtained from NASA SPDF database (http://www.spase-group.org/registry/render?f=yes&id=spase://VSPO/NumericalData/ISS/AMS-02/P27D). Data of NMs count rates were obtained from http://cosmicrays.oulu.fi (Oulu NM), http://pgia.ru/CosmicRay/ (Apatity), Neutron Monitor Database (NMDB), and IZMIRAN Cosmic Ray database (http://cr0.izmiran.ru/common/links.htm). NMDB database (www.nmdb.eu), founded under the European Union's FP7 Programme (Contract 213007), is not responsible for the data quality. PIs and teams of the experiments whose data were used here are gratefully acknowledged. Rolf Bütikofer is acknowledged for additional information on the local environmental conditions for JUN1 detectors. This work was partially supported by the Academy of Finland (ReSoLVE Centre of Excellence, Project 307411; HEAIM Projects 314982 and 316223; ESPERA Project 321882), by RFBR (Research Project 18-32-00062), RFBR and NRF (Research Project 19-52-60003), and MEPhI Academic Excellence Project (Contract 02.a03.21.0005), as well as by the International Space Science Institute support to International Team 441: High EneRgy sOlar partICle Events Analysis (HEROIC).

References

Abunin, A. A., Pletnikov, E. V., Shchepetov, A. L., & Yanke, V. G. (2011). Efficiency of detection for neutron detectors with different geometries. *Bulletin of the Russian Academy of Sciences: Physics*, *75*, 866–868. https://doi.org/10.3103/S1062873811060037

Agostinelli, S., Allison, J., Amako, K., Apostolakis, J., Araujo, H., Arce, P., & Zschiesche, D. (2003). Geant4-a simulation toolkit. *Nuclear Instruments and Methods in Physics Research A*, *506*, 250–303.

Aguilar, M., Ali Cavasonza, L., Alpat, B., Ambrosi, G., Arruda, L., Attig, N., & Zuccon, P. (2018). Observation of fine time structures in the cosmic proton and helium fluxes with the alpha magnetic spectrometer on the international space station. *Physical Review Letters*, *121*, 51101. https://doi.org/10.1103/PhysRevLett.121.051101

Bieber, J., Clem, J., Evenson, P., Oh, S., & Pyle, R. (2013). Continued decline of South Pole neutron monitor counting rate. *Journal of Geophysical Research*, *118*, 6847–6851. https://doi.org/10.1002/2013JA018915

Caballero-Lopez, R., & Moraal, H. (2012). Cosmic-ray yield and response functions in the atmosphere. *Journal of Geophysical Research*, *117*, A12103. https://doi.org/10.1029/2012JA017794

Clem, J., & Dorman, L. (2000). Neutron monitor response functions. *Space Science Reviews*, *93*, 335–359. https://doi.org/10.1023/A:1026508915269

Cooke, D., Humble, J., Shea, M., Smart, D., Lund, N., Rasmussen, I., & Petrou, N. (1991). On cosmic-ray cut-off terminology. *Nuovo Cimento C*, *14*, 213–234.

Debrunner, H., & Brunberg, E. Å. (1968). Monte Carlo calculation of the nucleonic cascade in the atmosphere. *Canadian Journal of Physics Supplements*, *46*, 1069–1072.

Desorgher, L., Flückiger, E. O., Gurtner, M., Moser, M. R., & Bütikofer, R. (2005). Atmocosmics: A Geant 4 code for computing the interaction of cosmic rays with the Earth's atmosphere. *International Journal of Modern Physics A*, *20*, 6802–6804. https://doi.org/10.1142/S0217751X05030132

Engel, R., Heck, D., & Pierog, T. (2011). Extensive air showers and hadronic interactions at high energies. *Annual Review of Nuclear and Particle Science*, *61*, 467–489.

Flückiger, E. O., Moser, M. R., Pirard, B., Bütikofer, R., & Desorgher, L. (2008). A parameterized neutron monitor yield function for space weather applications, *30th Proc. Internat. Cosmic Ray Conf. 2007* (vol. 1, pp. 289–292). Mexico City, Mexico: Universidad Nacional Autónoma de México.

Gil, A., Usoskin, I. G., Kovaltsov, G. A., Mishev, A. L., Corti, C., & Bindi, V. (2015). Can we properly model the neutron monitor count rate? *Journal of Geophysical Research: Space Physics*, *120*, 7172–7178. https://doi.org/10.1002/2015JA021654

Hatton, C. J., & Carimichael, H. (1964). Experimental investigation of the NM-64 neutron monitor. *Canadian Journal of Physics*, *42*, 2443–2472. https://doi.org/10.1139/p64-222

Koldobskiy, S. A., Bindi, V., Corti, C., Kovaltsov, G. A., & Usoskin, I. G. (2019). Validation of the neutron monitor yield function using data from AMS-02 experiment 2011–2017. *Journal of Geophysical Research: Space Physics*, *124*, 2367–2379. https://doi.org/10.1029/2018JA026340

Koldobskiy, S. A., Kovaltsov, G. A., & Usoskin, I. G. (2018). A solar cycle of cosmic ray fluxes for 2006–2014: Comparison between PAMELA and neutron monitors. *Journal of Geophysical Research: Space Physics*, *123*, 4479–4487. https://doi.org/10.1029/2018JA025516

Lockwood, J. A., Webber, W. R., & Hsieh, L. (1974). Solar flare proton rigidity spectra deduced from cosmic ray neutron monitor observations. *Journal of Geophysical Research*, *79*, 4149–4155. https://doi.org/10.1029/JA079i028p04149

Mangeard, P. S., Ruffolo, D., Sáiz, A., Madlee, S., & Nutaro, T. (2016). Monte Carlo simulation of the neutron monitor yield function. *Journal of Geophysical Research*, *121*, 7435–7448. https://doi.org/10.1002/2016JA022638

Maurchev, E., & Balabin, Y. (2016). Ruscosmic—The new software toolbox for detailed analysis of cosmic ray interactions with matter. *Solar-Terrestrial Physics*, *2*(4), 3–8. https://doi.org/10.12737/21289

Mavromichalaki, H., Papaioannou, A., Plainaki, C., Sarlanis, C., Souvatzoglou, G., Gerontidou, M., & Pustil'Nik, L. (2011). Applications and usage of the real-time Neutron Monitor Database. *Advances in Space Research*, *47*, 2210–2222. https://doi.org/10.1016/j.asr.2010.02.019

Mishev, A., Usoskin, I., & Kovaltsov, G. (2013). Neutron monitor yield function: New improved computations. *Journal of Geophysical Research: Space Physics*, *118*, 2783–2788. https://doi.org/10.1002/jgra.50325

Moraal, H., Belov, A., & Clem, J. M. (2000). Design and co-ordination of multi-station international neutron monitor networks. *Space Science Reviews*, *93*, 285–303. https://doi.org/10.1023/A:1026504814360

Nagashima, K., Sakakibara, S., Murakami, K., & Morishita, I. (1989). Response and yield functions of neutron monitor, galactic cosmic-ray spectrum and its solar modulation, derived from all the available world-wive surveys. *Nuovo Cimento C*, *12*, 173–209. https://doi.org/10.1007/BF02523790

Nuntiyakul, W., Sáiz, A., Ruffolo, D., Mangeard, P. S., Evenson, P., Bieber, J., & Humble, J. (2018). Bare neutron counter and neutron monitor response to cosmic rays during a 1995 latitude survey. *Journal of Geophysical Research: Space Physics*, *123*, 7181–7195. https://doi.org/10.1029/2017JA025135

Picone, J. M., Hedin, A. E., Drob, D. P., & Aikin, A. C. (2002). NRLMSISE-00 empirical model of the atmosphere: Statistical comparisons and scientific issues. *Journal of Geophysical Research*, *107*, 1468. https://doi.org/10.1029/2002JA009430

Pierog, T. (2017). Open issues in hadronic interactions for air showers. *EPJ Web of Conferences*, *145*, 18002. https://doi.org/10.1051/epjconf/201614518002

Simpson, J. A. (2000). The cosmic ray nucleonic component: The invention and scientific uses of the neutron monitor. *Space Science Reviews*, *93*, 11–32. https://doi.org/10.1023/A:1026567706183

Smart, D. F., Shea, M. A., Tylka, A. J., & Boberg, P. R. (2006). A geomagnetic cutoff rigidity interpolation tool: Accuracy verification and application to space weather. *Advances in Space Research*, *37*, 1206–1217. https://doi.org/10.1016/j.asr.2006.02.011

Stoker, P. H., Dorman, L. I., & Clem, J. M. (2000). Neutron monitor design improvements. *Space Science Reviews*, *93*, 361–380. https://doi.org/10.1023/A:1026560932107

Usoskin, I. G., Gil, A., Kovaltsov, G. A., Mishev, A. L., & Mikhailov, V. V. (2017). Heliospheric modulation of cosmic rays during the neutron monitor era: Calibration using PAMELA data for 2006–2010. *Journal of Geophysical Research: Space Physics*, *122*, 3875–3887. https://doi.org/10.1002/2016JA023819

Usoskin, I. G., & Kovaltsov, G. A. (2006). Cosmic ray induced ionization in the atmosphere: Full modeling and practical applications. *Journal of Geophysical Research*, *111*, D21206. https://doi.org/10.1029/2006JD007150